JACS
JOURNAL OF THE AMERICAN CHEMICAL SOCIETY

Article

pubs.acs.org/JACS

Efficient Tailoring of Upconversion Selectivity by Engineering Local Structure of Lanthanides in Na_xREF_{3+x} Nanocrystals

Hao Dong,[†] Ling-Dong Sun,*[,†] Ye-Fu Wang,[†] Jun Ke,[†] Rui Si,[‡] Jia-Wen Xiao,[†] Guang-Ming Lyu,[†] Shuo Shi,[†] and Chun-Hua Yan*[,†]

[†]Beijing National Laboratory for Molecular Sciences, State Key Laboratory of Rare Earth Materials Chemistry and Applications, PKU-HKU Joint Laboratory in Rare Earth Materials and Bioinorganic Chemistry, College of Chemistry and Molecular Engineering, Peking University, Beijing 100871, China

[‡]Shanghai Synchrotron Radiation Facility, Shanghai Institute of Applied Physics, Chinese Academy of Sciences, Shanghai 201204, China

Supporting Information

ABSTRACT: Efficient tailoring of upconversion emissions in lanthanide-doped nanocrystals is of great significance for extended optical applications. Here, we present a facile and highly effective method to tailor the upconversion selectivity by engineering the local structure of lanthanides in Na_xREF_{3+x} nanocrystals. The local structure engineering was achieved through precisely tuning the composition of nanocrystals, with different [Na]/[RE] ([F]/[RE]) ratio. It was found that the lattice parameter as well as the coordination number and local symmetry of lanthanides changed with the composition. A significant difference in the red to green emission ratio, which varied from 1.9 to 71 and 1.6 to 116, was observed for Na_xYF_{3+x}:Yb,Er and Na_xGdF_{3+x}:Yb,Er nanocrystals, respectively. Moreover, the local structure-dependent upconversion selectivity has been verified for Na_xYF_{3+x}:Yb,Tm nanocrystals. In addition, the local structure induced upconversion emission from Er^{3+} enhanced 9 times, and the CaF_2 shell grown epitaxially over the nanocrystals further promoted the red emission by 450 times, which makes it superior as biomarkers for *in vivo* bioimaging. These exciting findings in the local structure-dependent upconversion selectivity not only offer a general approach to tailoring lanthanide related upconversion emissions but also benefit multicolor displays and imaging.

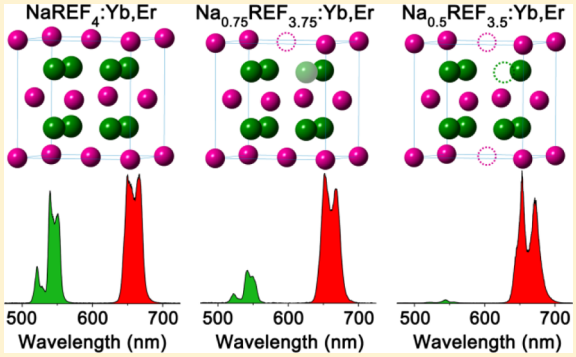

INTRODUCTION

Multicolor imaging and multiplexed detection gain tremendous concern in life science due to the capability of identifying and quantifying specific biological species with minimial amounts of sample and time cost.[1−3] Exploring novel optical markers to meet application requirements still remains a great challenge. In recent years, upconversion emissions from lanthanide-doped nanocrystals (NCs) have evoked extensive attention due to their fascinating anti-Stokes spectral character and great promises for bioimaging and therapy.[4−12] Furthermore, upconversion emissions from various lanthanides are significant in multicolor imaging and multiplexed detection.[13−16] Due to the abundant but invariant energy levels in 4f configurations, the resulting upconversion emissions are multiplex in spectra but fixed in wavelengths. Therefore, the crucial factor behind the feasibility of multiplexed applications is efficient modulation of the upconversion emission selectivity.[13]

For rare earth (RE) sodium fluorides, $NaREF_4$:Yb,Er NCs, which are one of the most efficient photon upconverting supporters,[17−19] the red emission ($^4F_{9/2} \rightarrow {}^4I_{15/2}$) of Er^{3+} is usually accompanied by the competitive green one ($^2H_{11/2}$, $^4S_{3/2} \rightarrow {}^4I_{15/2}$), yielding a yellow output in the cubic phase or under intense excitation.[20,21] The limitation in emission selectivity impedes the progress of multiplexed applications. To address the problem, a series of modulation strategies have been developed, which basically fall into three categories, controlling the lanthanide-doping concentration,[22−24] incorporating extrinsic energy levels from other lanthanides or transition-metal ions,[25−27] and constructing FRET systems by introducing acceptors within the particle building blocks.[28−31] However, adverse effects occur simultaneously with the above approaches. Excess amount of luminescent centers, including lanthanide or transition-metal ions, would lead to over-deleterious nonradiative cross-relaxations and thus decrease the upconversion emissions. As for the FRET system, besides the tedious fabrication process, the energy transfer is not efficient. Therefore, great challenges are still in front of the efficient modulation of upconversion selectivity.

Strikingly, it can be noticed that the upconversion selectivity differs greatly in different materials, and the structure-dependent upconversion emission behaviors should be studied.

Received: February 15, 2015
Published: May 4, 2015

DOI: 10.1021/jacs.5b01718
J. Am. Chem. Soc. 2015, 137, 6569−6576

Recently, Liu and co-workers demonstrated that energy clustering at sublattice level in KYb_2F_7:Er NCs is crucial for enhancing the multiphoton violet upconversion emission of Er^{3+}.[32] Aiming at engineering the red to green emission ratio (R/G) of Er^{3+}, optically inert ions, e.g., Li^+, were incorporated into Yb^{3+}–Er^{3+} codoped compounds to tailor the local symmetry of Er^{3+}.[33,34] However, spectral results exhibited little change in the R/G of Er^{3+}, ranging from ~0.3 to ~1.[33] Apart from that, the local structure of Er^{3+} can be affected by the external electric field via ferroelectric $BaTiO_3$:Yb,Er thin films,[35] and the R/G of Er^{3+} could be tuned from ~0.4 to ~0.8. Therefore, further investigations to deepen the understanding of local structure-dependent upconversion emission behaviors should be carried out urgently.

In this work, we develop a novel, facile, and highly effective method to tailor the upconversion selectivity of lanthanides by engineering the local structure of luminescent centers in nanocrystals. We employed stoichiometric $NaYF_4$:Yb,Er NCs as the reference and precisely tuned the composition, resulting in a series of nonstoichiometric Na_xYF_{3+x}:Yb,Er NCs with distinctive upconversion emission behaviors. Specifically, the local structure engineering is achieved by varying the molar ratio of [Na]/[RE] ([F]/[RE]), while the proportion of luminescent centers (Yb^{3+} and Er^{3+}) remains the same. As a result, the R/G of Er^{3+} changed significantly, ranging from ~2 to ~100, with the color output from yellow to red. Moreover, the near-infrared (NIR) to red emission ratio of Tm^{3+} changed greatly from ~38 to ~96 with the same strategy. In addition, the overall emission intensity enhanced benefiting from the local structural engineering and further promoted by 450 times with an epitaxial growth of biocompatible CaF_2 shells, leading to promising *in vitro* and *in vivo* bioimaging applications.

RESULTS AND DISCUSSION

All the samples were synthesized with a modified thermal decomposition method in a mixture of oleylamine (OM) and oleic acid (OA) at 280 °C for 15 min.[36−38] The local structure of lanthanides depends on the composition of the NCs, thus we began with precise tuning of the dosage of precursors, in which Na^+- and F^--containing precursors could be adjusted independently. The doping concentration of Yb^{3+} and Er^{3+} ions was 20% and 2% for all samples, respectively. As shown in Table S1, samples S1, S2, and S3 were synthesized with monotonically increasing dosage of CH_3COONa, while F1, F2, and F3 were prepared with progressively elevated dosage of CF_3COO^-.

To determine the composition of as-prepared S1−S3, and F1−F3 NCs, the inductively coupled plasma-atomic spectroscopy (ICP-AES) analysis was carried out. As shown in Table 1, the change of compositions of NCs is consistent with the tendency of precursor dosage. The molar ratio of RE ions ([Y]:[Yb]:[Er]) was similar for all samples. Moreover, the increasing dosage of CH_3COONa in S1−S3 group results gradually increased [Na]/[RE]. On the other hand, with elevated dosage of CF_3COO^-, the molar ratio of [Na]/[RE] also increased progressively from samples F1 to F3. It can be found that sample F3 is the stoichiometric $NaYF_4$:Yb,Er NCs, while the others should be nonstoichiometric counterparts.

Table 1. ICP-AES Analysis of S1−S3, and F1−F3 NCs

sample	[Y]:[Yb]:[Er]	[Na]/[RE]
S1	37.7:11.4:1	0.49
S2	36.1:10.9:1	0.73
S3	36.5:10.7:1	0.84
F1	38.2:10.8:1	0.48
F2	38.5:11.3:1	0.72
F3	38.2:9.0:1	0.96

In an attempt to provide independent information on [F] content, X-ray photoelectron spectrometry (XPS) measurement was carried out. As shown in Table S2, the molar ratio of [F]/[RE] increased from S1 to S3 and from F1 to F3 and followed the same changing trend with [Na]/[RE]. Moreover, the tendency of [Na]/[RE] obtained from XPS analysis agreed with the results of ICP-AES (Table 1). It is noteworthy that [F] should not be precisely equal to [Na] + 3 due to the fact that the NCs are coated with charged oleate ligands, which can act as anionic species like F^-.[39] However, to distinguish the compositions more conveniently, a general formula of Na_xREF_{3+x} will be used. The above results indicated that the composition of Na_xYF_{3+x}:Yb,Er NCs was sensitive to the dosage of precursors, and tuning of both Na^+ and F^- contents is valid for controlling the composition of these NCs. Compared with the stoichiometric hexagonal $NaREF_4$ NCs,[40,41] it is convenient to tune the compositions of cubic Na_xREF_{3+x} NCs in a wide range.

As shown in Figure 1a−f, the transmission electron microscopy (TEM) images of S1−S3 and F1−F3 indicated

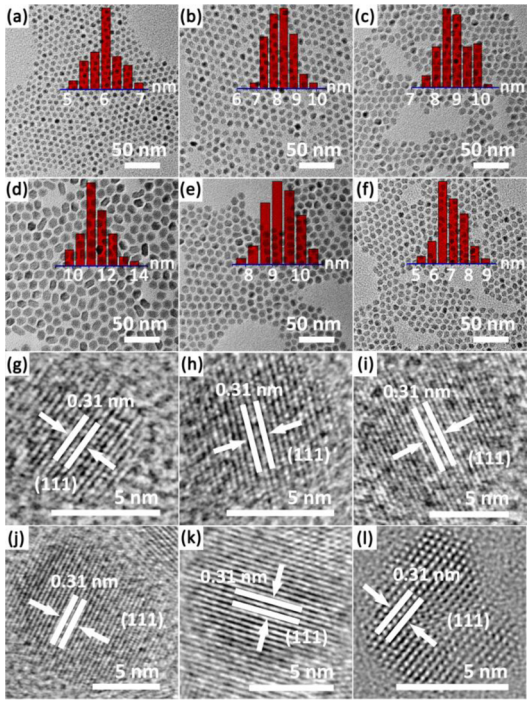

Figure 1. TEM images (a−f), corresponding size distributions (insets), and HRTEM images (g−l) of S1−S3, and F1−F3 NCs. (a−c, g−i) refer to samples S1−S3, and (d−f, j−l) refer to samples F1−F3.

all NCs are uniform in size and morphology. It can be noticed that the particle size differs in a regular manner. With increasing dosage of CH_3COONa from S1 to S3, the particle size was inclined to become larger (Figure 1a−c). As for samples with elevated dosage of CF_3COO^-, the particle size decreased gradually (Figure 1d−f). Typical high-resolution TEM images

DOI: 10.1021/jacs.5b01718
J. Am. Chem. Soc. 2015, 137, 6569−6576

of these NCs (Figure 1g–i) exhibited legible lattice distances of 0.31 nm, corresponding to the (111) spacing of cubic $NaYF_4$. This indicated that all the samples were crystallized with cubic phased structures.

To further uncover the crystal structural information, we carried out X-ray diffraction (XRD) measurements. As shown in Figure 2a, all samples could be assigned to cubic structure

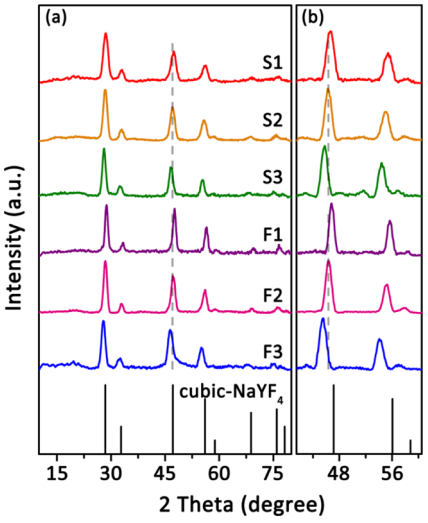

Figure 2. XRD patterns of S1–S3, F1–F3, and standard cubic-$NaYF_4$ (JCPDS 06-0342). The scanning speed was 8°/min for (a) and 1°/min for (b), respectively.

(JCPDS 06-0342) as referenced below, confirming the HRTEM results. Beyond that, an interesting phenomenon was found that the diffraction peaks from samples S3–S1 and F3–F1 shifted toward larger angles progressively, suggesting decreased lattice parameters for nonstoichiometric NCs. The slow-scanning XRD measurements (Figure 2b) were used to obtain the lattice parameters as listed in Table S3. It could be found that S3 and F3 possessed the largest lattice parameter of 5.56 and 5.61 Å among the samples. And as [Na]/[RE] ([F]/[RE]) reduced, the lattice parameters decreased. For samples S1 and F1, it decreased to 5.50 and 5.48 Å, respectively.

Except for the diffraction shift, difference in the diffraction broadening was also observed. As the dosage of CH_3COONa increased from S1 to S3, the diffraction peaks sharpened, indicating a gradual increase in particle size as evidenced in Figure 1a–c. Similarly, increasing the dosage of CF_3COO^- from F1 to F3, a progressive decrease in particle size (Figure 1d–f) was confirmed from the broadened diffraction peaks.

The upconversion spectra of these samples were recorded under the same condition. As shown in Figure 3a which are normalized at Er^{3+} green emissions, the R/G of Er^{3+} decreased significantly from S1 to S3 and from F1 to F3. The detailed R/G ratios (Figure 3b) and the corresponding digital photographs (Figure 3c) presented an intuitionistic insight into the emission. Apparently, stoichiometric $NaYF_4$:Yb,Er (F3) NCs produced a yellow emission with the smallest R/G of 1.9, which was quite similar to previous reports.[18,20] As the molar ratio of [Na]/[RE] ([F]/[RE]) reduced, the R/G enhanced greatly. It is worth noting that the R/G of S1 and F1 reached up to 34 and 71, respectively, giving out nearly spectrally pure red emissions. Although [Na]/[RE] is similar for S1 and F1, their R/G ratios are different for the green emission part of F1 is a little narrower than that of S1, which benefits the larger R/G for F1.

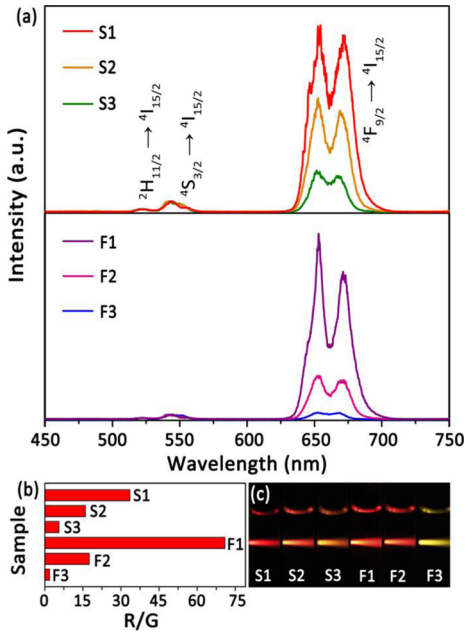

Figure 3. (a) Upconversion emission spectra (normalized at Er^{3+} 542 nm emissions) of S1–S3 and F1–F3 NCs upon 980 nm excitation with a power density of 10 W/cm^2. (b) R/G ratios and (c) digital photographs of samples S1–S3 and F1–F3.

Such spectral results revealed the difference in upconversion selectivity for Na_xYF_{3+x}:Yb,Er NCs.

As the size and size distributions were different for as-prepared NCs, evaluating the effect of size on upconversion emission selectivity is necessary. A series of stoichiometric $NaYF_4$:Yb,Er NCs with different size were prepared with epitaxial growth strategy to maintain the composition and the crystal structure (Table S4). As shown in Figure S1, the size of $NaYF_4$:Yb,Er NCs ranged from 7 to 13 nm and could cover those of S1–S3 and F1–F3. Spectral results (Figure S2) show that the R/G ratios of these samples exhibit a slight decrease from 1.9 to 1.5 and 1.6, which is consistent with the previous studies.[20] Therefore, the size difference on the upconversion selectivity can be ruled out.

The above structural and spectral characters of as-prepared NCs suggested a strong dependence of upconversion emission selectivity on the composition and lattice parameter. Since all these NCs are cubic structure, the change in composition and lattice parameter would result in different local structure around luminescent centers, which should be the dominant factor to account for the distinctive upconversion selectivity. Considering the reduced [Na]/[RE] ([F]/[RE]) and concomitant decreased lattice parameters of nonstoichiometric NCs, an appropriate amount of Na^+ and F^- vacancies should exist. And the upconversion energy-transfer processes in nonstoichiometric NCs may differ from that in stoichiometric $NaYF_4$:Yb,Er counterparts.

Aiming at investigating the local coordination structure, the extended X-ray absorption fine structure (EXAFS) measurements were performed. Because of the similar ionic radii and random occupation of cations, the local structure of Y^{3+} ions could be used to analyze that of Yb^{3+} and Er^{3+} ions. The X-ray absorption near edge structure (XANES) spectra, *k*-space (3.7–11.6 Å^{-1}, k^2-weighted), and *r*-space (1.32–2.22 Å, Y–F shell) EXAFS spectra of Y K-edge for the as-prepared NCs are depicted in Figures S3, S4, and 4, respectively. The

DOI: 10.1021/jacs.5b01718
J. Am. Chem. Soc. 2015, 137, 6569–6576

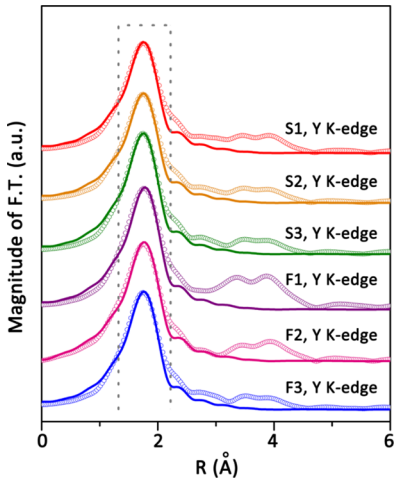

Figure 4. Experimental (dots) and Fourier transform fitting results (solid lines) of Y K-edge EXAFS spectra of S1−S3, and F1−F3 NCs. The window represents the range of *r*-space involved in the fit.

coordination number (CN) of Y^{3+}, average Y−F interatomic distance (R), Debye−Waller factor (DW), and ΔE_0 from the curve fitting of *r*-space EXAFS spectra are listed in Tables 2 and

Table 2. EXAFS Parameters of Y^{3+} in S1−S3 and F1−F3

sample	shell	CN	sample	shell	CN
S1	Y−F	7.1	F1	Y−F	6.9
S2	Y−F	7.7	F2	Y−F	7.3
S3	Y−F	7.9	F3	Y−F	7.9

S5. It can be found that there is a certain extent of overlap for the EXAFS parameters of Y^{3+} in Y−F shell if considering related uncertainties, implying the short-range structure similarity for the first Y−F shell. A slight increase might be appropriate to describe the CN values from S1 to S3 and from F1 to F3. As the amounts of vacancies gradually decreased with increasing [Na]/[RE] or [F]/[RE], it is reasonable for a slightly increased CN for Y^{3+} in Y−F shell from S1 to S3 and F1 to F3.

Besides the EXAFS measurements, luminescence from Ce^{3+} and Eu^{3+} was employed to reveal the difference in the local structure around lanthanides. Na_xYF_{3+x}:Ce (Ce1−Ce3, Tables S6 and S7, and Figures S5 and S6) and Na_xYF_{3+x}:Eu (Eu1−Eu3, Table S8 and S9, and Figure S7 and S8) NCs were synthesized with the same precursor adjusting strategy. For Na_xYF_{3+x}:Ce NCs because the typical 4f → 5d transition of Ce^{3+} is sensitive to local structure,[42] the shifts of luminescent spectra are correlated with the local structure around Ce^{3+}. As shown in Figure S6, the excitation and emission spectra of Ce^{3+} ions for nonstoichiometric Ce1 and Ce3 samples red-shifted obviously compared with those of stoichiometric Ce2 NCs. This indicated a decreased energy gap between the 4f and 5d levels of Ce^{3+} in Ce1 and Ce3 compared with that in Ce2. In addition, the full width at half-maximum for spectra of Ce1 and Ce3 is larger than that of Ce2, suggesting the stronger nephelanxetic effect in Ce1 and Ce3.[43] Therefore, the degree of covalence of Ce−F bonds should increase as the [Na]/[RE] ([F]/[RE]) decreased, which is well correlated to the increased Na^+ and F^- vacancies around Ce^{3+}.

For Na_xYF_{3+x}:Eu NCs, the ratio of electric-dipole emission at 615 nm to magnetic-dipole one at 590 nm is correlated with the local symmetry difference,[44] and the transition probability of lanthanides can be promoted with a reduced local symmetry for the partly released forbidden transitions.[45,46] For nonstoichiometric Eu1 and Eu3 samples (Figure S8), the emission ratios of 615 to 590 nm were both 3.1, larger than that of the stoichiometric one (1.6). This indicated a lower local symmetry around Eu^{3+} in Eu1 and Eu3 compared with that in Eu2.

Based on the above analyses, moderate amounts of Na^+ and F^- vacancies should exist as [Na]/[RE] ([F]/[RE]) reduced (Scheme 1), thus leading to lattice shrinkage, slightly decreased

Scheme 1. Schematic Illustration of (a) $NaYF_4$:Yb,Er and (b) $Na_{0.5}YF_{3.5}$:Yb,Er NCs in a Unit Cell

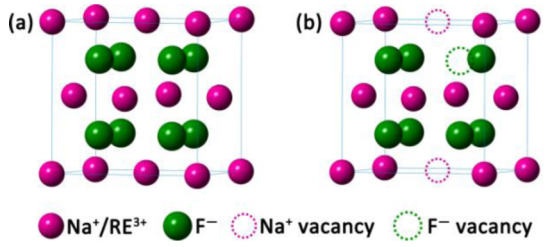

CN of RE^{3+} ions in RE−F shell, and lower local symmetry around luminescent centers. These would induce more intense interactions between lanthanides in nonstoichiometric NCs and further acted on the luminescence.

To probe the effect of local vacancies on the overall upconversion emission intensity, all of spectral measurements (Figure S9) were taken with consistent Yb^{3+} and Er^{3+} concentration (0.01 M). It can be found that sample F1 possesses the overwhelmingly superiority in intensity, and the emission from stoichiometric $NaYF_4$:Yb,Er (F3) NCs was less efficient than those from nonstoichiometric NCs. Beyond that, the enhancement in red emission and simultaneous reduction in green emission were observed for nonstoichiometric NCs. This could be correlated with the energy-transfer pathways which facilitated the population of red-emitting $^4F_{9/2}$ state and simultaneous depopulation of the green-emitting $^2H_{11/2}$ and $^4S_{3/2}$ states.

The excitation power-dependent emission intensity diagrams (Figure S10) indicated that both the green and red emissions in all NCs are derived from two-photon upconversion processes (Figure 5).[47] However, the spectral results indicated that the energy-transfer efficiency as well as additional population of the red-emitting $^4F_{9/2}$ state of Er^{3+} should be intensified in nonstoichiometric NCs owing to the vacancies.

Matching of the energy between donor and acceptor is one of the prerequisites for energy transfer. On this basis, both multiphoton cross-relaxations between two Er^{3+} ions (Figure S11) and between Er^{3+} and Yb^{3+} (Figure 5) may be reasons for enhanced R/G in nonstoichiometric NCs. However, the energy-transfer rate should also be considered. Energy transfer from states that lie closely above another one is unlikely due to its rapid depletion, and the multiphoton cross-relaxations between two Er^{3+} (Figure S11) should contribute less. By contrast, the cross-relaxation between Er^{3+} and Yb^{3+}, $^4S_{3/2}$ (Er^{3+}) + $^2F_{7/2}$ (Yb^{3+}) → $^4I_{13/2}$ (Er^{3+}) + $^2F_{5/2}$ (Yb^{3+}), should be the main reason to account for the enhanced R/G here, with a subsequent upward transition of $^4I_{13/2}$ → $^4F_{9/2}$ in Er^{3+}. This process has also been argued for enhanced R/G in many previous studies because the population of $^2F_{7/2}$ of Yb^{3+} is more practical than any other acceptor.[32,48,49]

DOI: 10.1021/jacs.5b01718
J. Am. Chem. Soc. 2015, 137, 6569−6576

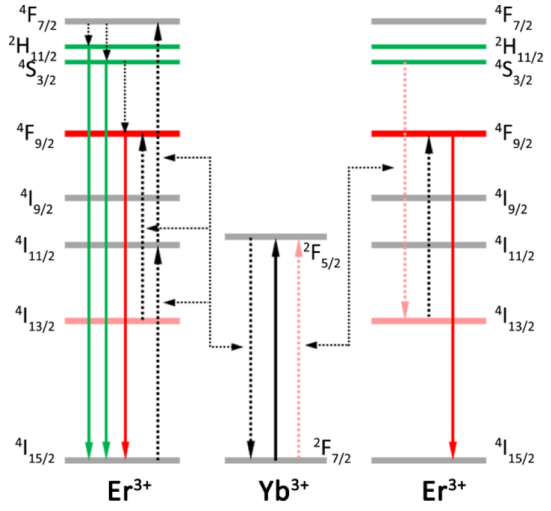

Figure 5. Proposed two-photon energy transfer from Yb^{3+} to Er^{3+} (left) and cross-relaxation between Er^{3+} and Yb^{3+} (right). Only partial energy states of Er^{3+} are shown for clarity. The green-, red-, and intermediate red-emitting excited states of Er^{3+} are highlighted in green, red, and light-red, respectively, and the cross-relaxation between Er^{3+} and Yb^{3+} is shown in light-red dotted lines.

In order to validate the general applicability of efficient tailoring of upconversion selectivity by engineering the local structure around luminescent centers, we further investigated the upconversion emission behaviors of Na_xYF_{3+x}:Yb,Tm and Na_xGdF_{3+x}:Yb,Er NCs. As depicted in Figure 6, the

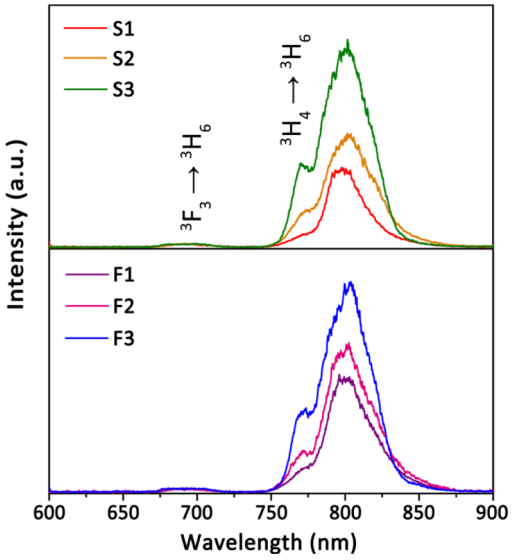

Figure 6. Upconversion emission spectra (normalized to Tm^{3+} 695 nm emissions) of Na_xYF_{3+x}:Yb,Tm NCs in cyclohexane colloidal solutions upon 980 nm excitation with the power density of 10 W/cm^2. The doping concentration of Yb^{3+} and Tm^{3+} was 20% and 1%, respectively.

upconversion selectivity of Tm^{3+} also depends on the composition of NCs. As the molar ratio of [Na]/[RE] ([F]/[RE]) reduced from S3 to S1 and F3 to F1, the NIR (800 nm, $^3H_4 \rightarrow {}^3H_6$) to red (695 nm, $^3F_3 \rightarrow {}^3H_6$) emission ratios of Tm^{3+} decreased greatly from 96 to 38 and from 95 to 60, respectively. Such a phenomenon might be attributed to the decreased nonradiative relaxation rate of $^3F_3 \rightarrow {}^3H_4$ of Tm^{3+} in nonstoichiometric NCs (Figure S12). As for the Na_xGdF_{3+x}:Yb,Er NCs (Table S10), the resulting composition (Table S11), size distribution (Figures S13 and S14), and upconversion emission spectra (Figure S15) showed the same changing trend as that of Na_xYF_{3+x}:Yb,Er NCs. Stoichiometric $NaGdF_4$:Yb,Er NCs exhibited the smallest R/G of 1.6, while it increased gradually with reduced [Na]/[RE] ([F]/[RE]) in nonstoichiometric NCs. Therefore, these results indicated the general applicability of the local structure-dependent upconversion selectivity.

Due to the lower scattering and location in the first biological window, red emission is more favorable for the bioimaging applications than green one.[26,50] On this basis, nearly spectral pure, intense red emitting F1 NCs should be a decent choice for bioimaging. To further enhance the red emission, biocompatible CaF_2 shell was introduced via epitaxial growth. Apart from the enhancement effect, the CaF_2 layer can also suppress the leakage of RE^{3+} ions, ensuring the biosafety of F1@CaF_2 NCs.[51]

TEM image (Figure 7a) showed that the F1@CaF_2 core/shell NCs are uniform in size and morphology. And legible

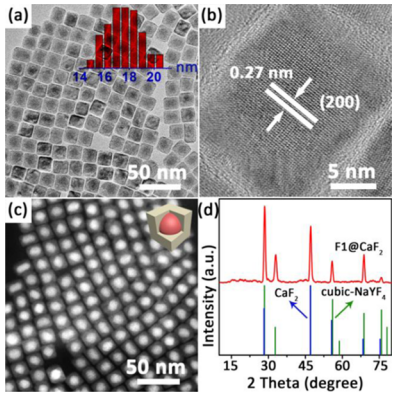

Figure 7. TEM image (a), HRTEM image (b), HAADF-STEM image (c), and XRD pattern (d) of F1@CaF_2 NCs. Standard CaF_2 (JCPDS 01-1274) and α-$NaYF_4$ (JCPDS 06-0342) patterns are also shown in (d).

lattice distance of 0.27 nm can be observed (Figure 7b), corresponding to the (200) plane of CaF_2. Furthermore, the high-angle annular dark-field scanning transmission electron microscopy (HAADF-STEM) verified the core/shell structure through image contrast (Figure 7c). The inner brighter part corresponds to heavier elements, Y, Yb, and Er, in core parts, while the outer darker part is relevant to lighter one, Ca, in CaF_2 shells. The XRD pattern of F1@CaF_2 NCs (Figure 7d) corresponds well with the standard patterns of CaF_2 and cubic $NaYF_4$, confirming the HRTEM results.

The red emission of F1@CaF_2 increased by 450 times compared with that of F1 (Figure 8a). An obvious R/G decrease was observed for the changed local structure with F^- feeding during the epitaxial growth. Even though, the red emission dominated the visible region. Compared with larger hexagonal $NaYF_4$:Yb,Er NCs (~50 nm) and stoichiometric F3@CaF_2 NCs (Figures S16 and S17), F1@CaF_2 NCs possess the strongest red and overall upconversion emissions (Figure 8a). Corresponding integrated intensity diagram (Figure 8b) and digital luminescence photographs (Figure 8c) showed the superiority of F1@CaF_2 NCs in upconversion emissions. It is also noteworthy that upconversion emission from F1@CaF2

DOI: 10.1021/jacs.5b01718
J. Am. Chem. Soc. 2015, 137, 6569−6576

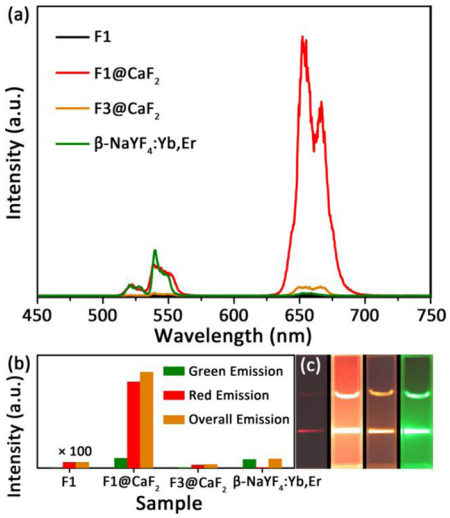

Figure 8. Upconversion emission spectra (a), integrated intensity diagram (b), and digital luminescence photographs (c) of F1, F1@CaF_2, F3@CaF_2, and β-$NaYF_4$:Yb,Er NCs with the same concentration of luminescent centers (Yb^{3+} and Er^{3+}) of 5 mM upon 980 nm excitation. The excitation power density was 500 mW/cm^2. The photographs were taken with exposure times of 3 s.

NCs is ~12 times more intense than that from 26 nm hexagonal core/shell NCs (Figure S18). In addition, we assessed the absolute quantum yields (QYs) of these NCs. Upon 0.6 W/cm^2 excitation, the QY of F1@CaF_2 NCs is 0.012%, which is 2 orders of magnitude higher than that of other samples and reaches the same order of magnitude to the QYs of hexagonal $NaYF_4$:Yb,Er NCs obtained by van Veggel et al.[52] Upon 130 W/cm^2 excitation, the QY of F1@CaF_2 NCs reaches 1.42% and is still higher than that of F3@CaF_2 (1.07%) and β-$NaYF_4$:Yb,Er (0.99%) NCs. Due to the different saturation regime, hexagonal core/shell NCs can release more intense upconversion emissions with a QY of 2.88%, which is similar to the QY of $LiLuF_4$:Yb,Er core/shell NCs.[53] However, considering the bioapplications with low power excitation, F1@CaF_2 NCs is more suitable for bioimaging.

After ligand exchange to hydrophobic NCs (Figure S19), spectrally pure red emission recovered due to the prominent quenching of green one by hydroxyl groups (Figure S20).[54] The cytotoxicity assessments showed that <10% of the A549 cells died following incubation with F1@CaF_2 NCs (200 μg/mL) for 24 h (Figure S21), which is supposed to be less cytotoxic[55,56] and much better than that of CdSe quantum dots.[57] The confocal laser scanning image showed that A549 cells exhibited intense emission at the red channel (λ = 644−650 nm) (Figure S22) under 980 nm excitation, indicating that the F1@CaF_2 NCs are excellent for cellular imaging.

Penetration depth experiments were next carried out for the promise of *in vivo* imaging. Green-emitting hexagonal $NaYF_4$:Yb,Er NCs (~50 nm) were adopted for comparison. We monitored the upconversion emission spectra by adding mutton slices both on the incident and emissive light path. It can be found that F1@CaF_2 NCs exhibit stronger emissions than the hexagonal $NaYF_4$:Yb,Er NCs (Figure S23). In addition, green emission decreased faster than red one due to the scattering effect, which has an inverse relationship to the fourth power of wavelength. The red-emitting F1@CaF_2 NCs can penetrate more layers than the green emitting $NaYF_4$:Yb,Er NCs. Furthermore, we performed the *in vitro* experiments by injecting the same amount of NCs into chicken breast tissue at a different depth. It was found that upconversion signals from F1@CaF_2 NCs can be collected at a depth over 10 mm (Figure S24). However, the green-emitting hexagonal $NaYF_4$:Yb,Er NCs can only penetrate over 4 mm or so.

In vivo imaging was demonstrated with a nude mouse and a Kunming mouse, respectively. It was found that photons collected from F1@CaF_2 NCs (right) were found to be twice more than those of hexagonal $NaYF_4$:Yb,Er (left) NCs (Figure 9a) and 4.5 times more than those from 26 nm hexagonal core/

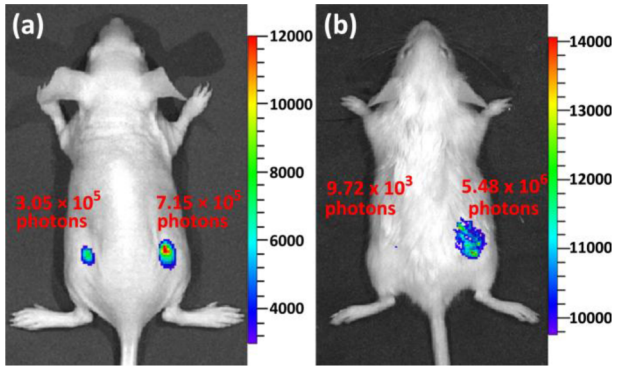

Figure 9. *In vivo* upconversion luminescence imaging of a nude mouse (a) and Kunming mouse (b) with hexagonal $NaYF_4$:Yb,Er NCs (left back side) and F1@CaF_2 NCs (right back side) by subcutaneously injection (30 μL (a) and 20 μL (b) of 5 mg/mL aqueous colloids, respectively). Excitation power density for (a, b) was 200 and 500 mW/cm^2, respectively. Exposure time for (a, b) was 0.1 and 0.2 s, respectively.

shell NCs (Figure S25). It is well-known that the mouse hair plays a key role in the absorption and scattering of excitation and emission lights. As shown in Figure 9b, the photons collected from F1@CaF_2 NCs (right) were 2 orders of magnitude more than those from hexagonal $NaYF_4$:Yb,Er NCs (left). These results confirmed the superiority of F1@CaF_2 NCs with intense red emission for *in vivo* imaging studies.

■ CONCLUSION

In summary, we have developed a novel, facile, and highly effective method to tailor upconversion selectivity by engineering the local structure of lanthanides. For lanthanide-doped Na_xREF_{3+x} NCs, the local structure could be affected greatly by tuning the composition of NCs. Reduced [Na]/[RE] ([F]/[RE]) leads to decreased lattice parameters, decreased CN of RE^{3+} in the RE−F shell and lower local symmetry, accompanied by the emergence of Na^+/F^- vacancies. As a result, the upconversion selectivity changed notably. By this strategy, the R/G of Er^{3+} changed significantly from ~2 to ~100, and the NIR to red emission ratio of Tm^{3+} changed from ~38 to ~96. The local structure-dependent upconversion selectivity provides a general approach to tailor lanthanide upconversion emissions and is promising for multiplexed applications. Furthermore, the CaF_2 capped red-emitting core/shell NCs acted as effective biomarkers for *in vivo* imaging with remarkable penetration depths.

■ EXPERIMENTAL SECTION

Materials. RE oxides were purchased from China Rare Earth Online Co., Ltd. OA (>90%) and trifluoroacetic acid (99%) were procured from Sigma-Aldrich. OM (>80%) and trifluoroacetic acid

DOI: 10.1021/jacs.5b01718
J. Am. Chem. Soc. 2015, 137, 6569−6576

sodium salt (99%) were obtained from Acros. Sodium acetate (AR), citric acid (AR), acetic acid (AR), ethanol (AR), chloroform (AR), and cyclohexane (AR) were purchased from Beijing Chemical Works. Note that all the reagents were used as received without further purification.

Instrumentation. Samples for TEM examination were prepared by drying a drop of colloidal solution dispersed with NCs on a copper grid. Low-resolution TEM measurements were operated with a JEOL JEM-2100 TEM operated at 200 kV. HRTEM and HAADF-STEM measurements were performed with a JEOL JEM-2100F TEM operated at 200 kV. ICP-AES analysis was carried out with a Leeman Profile SPEC. Note that all the ICP-AES samples were digested in quartz tubes to avoid contaminants, especially Na^+ ions, leaching from the tubes. XPS was recorded on an Axis Ultra imaging photoelectron spectrometer (Kratos, U.K.). XRD patterns were recorded on a Rigaku D/MAX-2000 diffractometer (Japan), using Cu Kα radiation (λ = 1.5406 Å). Y K-edge EXAFS measurements were carried out on the BL14W1 beamline of Shanghai Synchrotron Radiation Facility (SSRF) operated at 3.5 GeV under "top-up" mode with currents of 220 mA. Data were collected with a monochromator using two flat Si(311) crystals (Y K-edge) under focusing mode. Harmonics were rejected by using a grazing incidence mirror if necessary. Y K-edge (17038 eV) absorption measurements were performed in transmission mode (I_0 and I_t two ion chambers). The energy calibration was monitored using a reference sample (bulk cubic phased Y_2O_3). Data processing and analysis were performed using the IFEFFIT package with Athena and Artemis softwares.[58,59] EXAFS analysis was done by fitting the theoretical functions of $NaREF_4$ calculated with FEFF6 to the experimental data in *r*-space. All the fitted data were limited to the first shell (RE−F) contribution. The passive electron factors, S_0^2, were set to 1 and then fixed for further analysis of the NCs. The parameters describing the electronic properties (e.g., correction to the photoelectron energy origin, ΔE_0) and local structure environment (CN, *R*, and DW factor) around the absorbing atoms were allowed to vary during the curve fitting process. The corresponding *k* weight in *k*-space was fixed to k^2- for Y K-edge. The related Δk and ΔR parameters were selected to be 3.7−11.6 $Å^{-1}$ and 1.32−2.22 Å, respectively. Photoluminescence spectra and upconversion spectra were monitored on a Hitachi F-4500 fluorescent spectrometer with the PMT voltage of 700 V. 980 nm lasers are high-power multimode pump lasers (Hi-tech Optoelectronic Co. Ltd., with a maximum power 5.0 W). The absolute QY measurements were performed with a FLS920 steady-state and time-resolved fluorescence spectrometer (Edinburgh Instruments), and emissions of 400−750 nm were integrated for the quantum efficiency determination.

Synthesis of Cubic Na_xREF_{3+x}:Yb,Er (RE = Y, Gd) NCs. Dosages of precursors for preparing NCs are shown in Tables S1 and S10. In a typical procedure, a given amount of precursors (1 mmol) was added to a mixture of OM and OA (20 mL, volume ratio 9:1) in a 100 mL three-necked flask at room temperature. The slurry was heated to 110 °C to remove oxygen and water with vigorous stirring. After that, a clear solution formed and was heated to 280 °C for 15 min with a heating rate of 15 °C/min under N_2 atmosphere. Upon cooling to room temperature, an excess amount of ethanol was added to precipitate the NCs. The products were collected by centrifugation at 7800 rpm for 10 min and then washed with ethanol for several times. Finally, the NCs were redispersed in 10 mL cyclohexane for characterizations.

Synthesis of Cubic Na_xYF_{3+x}:Ce and Na_xYF_{3+x}:Eu NCs. Dosages of precursors are listed in Tables S6 and S8, respectively. The synthetic procedure was similar to that of Yb^{3+}, Er^{3+}-doped NCs except that luminescent centers (Yb^{3+}, Er^{3+}) were replaced by Ce^{3+} or Eu^{3+}, respectively.

■ ASSOCIATED CONTENT

Supporting Information

Experimental details, more EXAFS spectra, TEM images, upconversion spectra, and other supplementary figures and tables. The Supporting Information is available free of charge on the ACS Publications website at DOI: 10.1021/jacs.5b01718.

■ AUTHOR INFORMATION

Corresponding Authors

*sun@pku.edu.cn

*yan@pku.edu.cn

Notes

The authors declare no competing financial interest.

■ ACKNOWLEDGMENTS

This work was supported by NSFC (Nos. 21425101, 21321001, 21371011, 21331001) and MOST of China (2014CB643800). We greatly thank Prof. Xueyuan Chen and Dr. Datao Tu at Fujian Institute of Research on the Structure of Matter, Chinese Academy of Sciences, for their valuable help in the absolute quantum yield measurements. We also greatly thank Prof. Ye Tao and Mr. Fei Zhan at Institute of High Energy Physics, Chinese Academy of Sciences, for their meritorious help in the EXAFS data analysis.

■ REFERENCES

(1) Schendure, J.; Porreca, G. J.; Reppas, N. B.; Lin, X. X.; McCutcheon, J. P.; Rosenbaum, A. M.; Wang, M. D.; Zhang, K.; Mitra, R. D.; Church, G. M. *Science* **2005**, *309*, 1728.

(2) Klostranec, J. M.; Xiang, Q.; Farcas, G. A.; Lee, J. A.; Rhee, A.; Lafferty, E. I.; Perrault, S. D.; Kain, K. C.; Chan, W. C. W. *Nano Lett.* **2007**, *7*, 2812.

(3) Lu, J.; Paulsen, I. T.; Jin, D. Y. *Anal. Chem.* **2013**, *85*, 8240.

(4) Auzel, F. *Chem. Rev.* **2004**, *104*, 139.

(5) van der Ende, B. M.; Aarts, L.; Meijerink, A. *Phys. Chem. Chem. Phys.* **2009**, *11*, 11081.

(6) Wang, F.; Liu, X. G. *Chem. Soc. Rev.* **2009**, *38*, 976.

(7) Zhou, J. C.; Yang, Z. L.; Dong, W.; Tang, R. J.; Sun, L. D.; Yan, C. H. *Biomaterials* **2011**, *32*, 9059.

(8) Zhou, J.; Liu, Z.; Li, F. Y. *Chem. Soc. Rev.* **2012**, *41*, 1323.

(9) Dong, H.; Sun, L. D.; Yan, C. H. *Nanoscale* **2013**, *5*, 5657.

(10) Liu, Y. S.; Tu, D. T.; Zhu, H. M.; Chen, X. Y. *Chem. Soc. Rev.* **2013**, *42*, 6942.

(11) Sun, L. D.; Wang, Y. F.; Yan, C. H. *Acc. Chem. Res.* **2014**, *47*, 1001.

(12) Gai, S. L.; Li, C. X.; Yang, P. P.; Lin, J. *Chem. Rev.* **2014**, *114*, 2343.

(13) Gorris, H. H.; Wolfbeis, O. S. *Angew. Chem., Int. Ed.* **2013**, *52*, 3584.

(14) Dou, Q. Q.; Idris, N. M.; Zhang, Y. *Biomaterials* **2013**, *34*, 1722.

(15) Lu, Y. Q.; Zhao, J. B.; Zhang, R.; Liu, Y. J.; Liu, D. M.; Goldys, E. M.; Yang, X. S.; Xi, P.; Sunna, A.; Lu, J.; Shi, Y.; Leif, R. C.; Huo, Y. J.; Shen, J.; Piper, J. A.; Robinson, J. P.; Jin, D. Y. *Nat. Photonics* **2013**, *8*, 32.

(16) Wang, F.; Liu, X. G. *Acc. Chem. Res.* **2014**, *47*, 1378.

(17) Menyuk, N.; Dwight, K.; Pierce, J. W. *Appl. Phys. Lett.* **1972**, *21*, 159.

(18) Heer, S.; Kömpe, K.; Güdel, H. U.; Haase, M. *Adv. Mater.* **2004**, *16*, 23.

(19) Suyer, J. F.; Grimm, J.; Krämer, K. W.; Güdel, H. U. *J. Lumin.* **2005**, *114*, 53.

(20) Mai, H. X.; Zhang, Y. W.; Sun, L. D.; Yan, C. H. *J. Phys. Chem. C* **2007**, *111*, 13721.

(21) Sun, L. D.; Dong, H.; Zhang, P. Z.; Yan, C. H. *Annu. Rev. Phys. Chem.* **2015**, *66*, 619.

(22) Vetrone, F.; Boyer, J.-C.; Capobianco, J. A.; Speghini, A.; Bettinelli, M. *J. Appl. Phys.* **2004**, *96*, 661.

(23) Wang, F.; Liu, X. G. *J. Am. Chem. Soc.* **2008**, *130*, 5642.

(24) Wei, W.; Zhang, Y.; Chen, R.; Goggi, J.; Ren, N.; Huang, L.; Bhakoo, K. K.; Sun, H. D.; Tan, T. T. Y. *Chem. Mater.* **2014**, *26*, 5183.

DOI: 10.1021/jacs.5b01718
J. Am. Chem. Soc. 2015, 137, 6569−6576

(25) Chen, G. Y.; Liu, H. C.; Somesfalean, G.; Liang, H. J.; Zhang, Z. G. *Nanotechnology* **2009**, *20*, 385704.
(26) Wang, J.; Wang, F.; Wang, C.; Liu, Z.; Liu, X. G. *Angew. Chem., Int. Ed.* **2011**, *50*, 10369.
(27) Chan, E. M.; Han, G.; Goldberg, J. D.; Gargas, D. J.; Ostrowski, A. D.; Schuck, P. J.; Cohen, B. E.; Milliron, D. J. *Nano Lett.* **2012**, *12*, 3839.
(28) Wang, L. Y.; Yan, R. X.; Huo, Z. Y.; Wang, L.; Zeng, J. H.; Bao, J.; Wang, X.; Peng, Q.; Li, Y. D. *Angew. Chem., Int. Ed.* **2005**, *44*, 6054.
(29) Li, Z. Q.; Zhang, Y.; Jiang, S. *Adv. Mater.* **2008**, *20*, 4765.
(30) Cheng, L.; Yang, K.; Shao, M. W.; Lee, S.-T.; Liu, Z. *J. Phys. Chem. C* **2011**, *115*, 2686.
(31) Gorris, H. H.; Ali, R.; Saleh, S. M.; Wolfbeis, O. S. *Adv. Mater.* **2011**, *23*, 1652.
(32) Wang, J.; Deng, R. R.; MacDonald, M. A.; Chen, B.; Yuan, J. K.; Wang, F.; Chi, D. Z.; Hor, T. S. A.; Zhang, P.; Liu, G. K.; Han, Y.; Liu, X. G. *Nat. Mater.* **2014**, *13*, 157.
(33) Chen, G. Y.; Liu, H. C.; Liang, H.; Somesfalean, G.; Zhang, Z. G. *J. Phys. Chem. C* **2008**, *112*, 12030.
(34) Cheng, Q.; Sui, J. H.; Cai, W. *Nanoscale* **2012**, *4*, 779.
(35) Hao, J. H.; Zhang, Y.; Wei, X. H. *Angew. Chem., Int. Ed.* **2011**, *50*, 6876.
(36) Mai, H. X.; Zhang, Y. W.; Si, R.; Yan, Z. G.; Sun, L. D.; You, L. P.; Yan, C. H. *J. Am. Chem. Soc.* **2006**, *128*, 6426.
(37) Boyer, J.-C.; Vetrone, F.; Cuccia, L. A.; Capobianco, J. A. *J. Am. Chem. Soc.* **2006**, *128*, 7444.
(38) Mai, H. X.; Zhang, Y. W.; Sun, L. D.; Yan, C. H. *J. Phys. Chem. C* **2007**, *111*, 13730.
(39) Gomes, R.; Hassinen, A.; Szczygiel, A.; Zhao, Q.; Vantomme, A.; Martins, J. C.; Hens, Z. *J. Phys. Chem. Lett.* **2011**, *2*, 145.
(40) Thoma, R. E.; Hebert, G. M.; Insley, H.; Weaver, C. F. *Inorg. Chem.* **1963**, *2*, 1005.
(41) Ostrowski, A. D.; Chan, E. M.; Gargas, D. J.; Katz, E. M.; Han, G.; Schuck, P. M.; Milliron, D. J.; Cohen, B. E. *ACS Nano* **2012**, *3*, 2686.
(42) Zhao, Y. M.; Rabouw, F. T.; van Puffelen, T.; van Walree, C. A.; Gamelin, D. R.; de Mello Donegá, C.; Meijerink, A. *J. Am. Chem. Soc.* **2014**, *136*, 16533.
(43) Ishii, Y.; Arai, K.; Namikawa, H.; Tanaka, M.; Negishi, A.; Handa, T. *J. Am. Ceram. Soc.* **1987**, *70*, 72.
(44) Tu, D. T.; Liu, Y. S.; Zhu, H. M.; Li, R. F.; Liu, L. Q.; Chen, X. Y. *Angew. Chem.* **2013**, *125*, 1166.
(45) Liu, G. K. *Chem. Soc. Rev.* **2015**, *44*, 1635.
(46) Dong, H.; Sun, L. D.; Yan, C. H. *Chem. Soc. Rev.* **2015**, *44*, 1608.
(47) Pollnau, M.; Gamelin, D. R.; Lüthi, S. R.; Güdel, H. U.; Hehlen, M. P. *Phys. Rev. B* **2000**, *61*, 3337.
(48) Anderson, R. B.; Smith, S. J.; May, P. S.; Berry, M. T. *J. Phys. Chem. Lett.* **2014**, *5*, 36.
(49) Zhang, J. H.; Hao, Z. D.; Li, J.; Zhang, X.; Luo, Y. S.; Pan, G. H. *Light: Sci. Appl.* **2015**, *4*, 239.
(50) Weissleder, R. *Nat. Biotechnol.* **2001**, *19*, 316.
(51) Wang, Y. F.; Sun, L. D.; Xiao, J. W.; Feng, W.; Zhou, J. C.; Shen, J.; Yan, C. H. *Chem.—Eur. J.* **2012**, *18*, 5558.
(52) Boyer, J. C.; van Veggel, F. C. J. M. *Nanoscale* **2010**, *2*, 1417.
(53) Huang, P.; Zheng, W.; Zhou, S. Y.; Tu, D. T.; Chen, Z.; Zhu, H. M.; Li, R. F.; Ma, E.; Huang, M. D.; Chen, X. Y. *Angew. Chem., Int. Ed.* **2014**, *53*, 1252.
(54) Bogdan, N.; Vetrone, F.; Ozin, G. A.; Capobianco, J. A. *Nano Lett.* **2011**, *11*, 835.
(55) Liu, Q.; Sun, Y.; Yang, T. S.; Feng, W.; Li, C. G.; Li, F. Y. *J. Am. Chem. Soc.* **2011**, *133*, 17122.
(56) Zheng, W.; Zhou, S. Y.; Chen, Z.; Hu, P.; Liu, Y. S.; Tu, D. T.; Zhu, H. M.; Li, R. F.; Huang, M. D.; Chen, X. Y. *Angew. Chem., Int. Ed.* **2013**, *52*, 6671.
(57) Derfus, A. M.; Chan, W. C. W.; Bhatia, S. N. *Nano Lett.* **2004**, *4*, 11.
(58) Newville, M. *J. Synchrotron Radiat.* **2001**, *8*, 322.
(59) Ravel, B.; Newville, M. *J. Synchrotron Radiat.* **2005**, *12*, 537.

DOI: 10.1021/jacs.5b01718
J. Am. Chem. Soc. 2015, 137, 6569−6576